Aalto University

OPEN ACCESS

This is an electronic reprint of the original article.
This reprint may differ from the original in pagination and typographic detail.

Pirsto, Ville; Kukkola, Jarno; Hinkkanen, Marko; Harnefors, Lennart

Intersample Modeling of the Converter Output Admittance

Published in:
IEEE Transactions on Industrial Electronics

DOI:
10.1109/TIE.2020.3029482

Published: 01/11/2021

Document Version
Peer-reviewed accepted author manuscript, also known as Final accepted manuscript or Post-print

Please cite the original version:
Pirsto, V., Kukkola, J., Hinkkanen, M., & Harnefors, L. (2021). Intersample Modeling of the Converter Output Admittance. *IEEE Transactions on Industrial Electronics*, *68*(11), 11348-11358. Article 9222485.
https://doi.org/10.1109/TIE.2020.3029482

This material is protected by copyright and other intellectual property rights, and duplication or sale of all or part of any of the repository collections is not permitted, except that material may be duplicated by you for your research use or educational purposes in electronic or print form. You must obtain permission for any other use. Electronic or print copies may not be offered, whether for sale or otherwise to anyone who is not an authorised user.

© 2020 IEEE. This is the author's version of an article that has been published by IEEE. Personal use of this material is permitted. Permission from IEEE must be obtained for all other uses, in any current or future media, including reprinting/republishing this material for advertising or promotional purposes, creating new collective works, for resale or redistribution to servers or lists, or reuse of any copyrighted component of this work in other works.

Inter-Sample Modeling of the Converter Output Admittance

Ville Pirsto, Jarno Kukkola, Marko Hinkkanen, *Senior Member, IEEE*, and Lennart Harnefors, *Fellow, IEEE*

***Abstract*—The stability of the converter–grid interconnection can be studied by analyzing the product of the converter output admittance and the grid impedance. For reliable stability analysis, it has been of interest to obtain accurate converter output admittance models for a wide range of frequencies, ideally also around and above the Nyquist frequency of the converter system. This paper presents a modeling method for the output admittance of power converters defined in the Laplace domain that takes into account the discrete nature of the control system. The modeling method is based on analyzing the inter-sample behavior of sampled-data systems, a class of systems which includes the modern digitally-controlled power converters. The proposed method is compared to conventional admittance modeling methods, and its accuracy is validated by means of simulations and experiments.**

***Index Terms*—Admittance modeling, Nyquist frequency, power converter, sampled-data system.**

I. Introduction

The penetration of power electronic converters in the electric grid has increased enormously during the last years. If the grid impedance seen by the converter is high, stability issues caused by the converter–grid interconnection might arise. The interconnection stability can be analyzed through the product of the converter output admittance Y_{oa} and the grid impedance Z_{g} (cf. Fig. 1) [1].

In practice, this stability analysis can be conducted by measuring [2]–[5] or modeling [6]–[12] the grid impedance and the converter output admittance. If the grid is unknown, the grid impedance can be estimated, e.g., as in [2]. Similarly, if the converter system is unknown, the converter output admittance can be measured [3]–[5]. However, additional hardware is typically required for the measurement [3]. Thus, measuring the admittance of a converter in the grid can be difficult or even impossible to carry out when the converter is in full operation and transferring energy to the grid, e.g., from a renewable energy source. Furthermore, the converter admittance typically depends on the operating point of the converter, and a significant number of measurements under different operating points are required in order to obtain a comprehensive overview of the converter admittance. On the other hand, if the converter system is known, modeling can be employed. This is desirable, as no special arrangements are required and the converter admittance can be evaluated in a wide range of operating points with little effort. Modeling can also be used to design controllers that result in a stable converter–grid interconnection [11].

Manuscript received March 6, 2020; revised July 3, 2020 and August 14, 2020; accepted September 19, 2020. This work was supported in part by ABB Oy and in part by Tekniikan edistämissäätiö.

V. Pirsto, J. Kukkola, and M. Hinkkanen are with the Department of Electrical Engineering and Automation, Aalto University, Espoo, Finland (email: ville.pirsto@aalto.fi; jarno.kukkola@aalto.fi; marko.hinkkanen@aalto.fi).

L. Harnefors is with the ABB Corporate Research, Västerås, Sweden, and also with the KTH Royal Institute of Technology, Stockholm, Sweden (email: lennart.harnefors@se.abb.com).

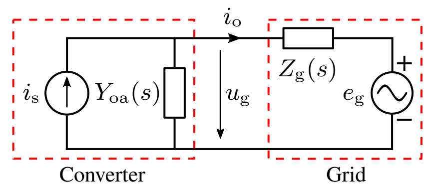

Fig. 1. Linearized model of a grid converter system. The converter is modeled as a current source i_{s} in parallel with an output admittance Y_{oa}. The grid is modeled as an ideal voltage source e_{g} in series with a grid impedance Z_{g}. The grid current is i_{o} and the voltage at the point of common coupling is u_{g}.

Conventionally, the output admittance of a converter has been modeled assuming the system to be purely continuous-time [6]–[12]. However, the control system of the converter is typically implemented on a digital processor that executes difference equations in the discrete-time domain. Thus, the converter system is actually a hybrid, where both continuous- and discrete-time signals exist. Due to this discrepancy between the assumptions and the reality, the purely continuous-time models may yield inaccurate results for some systems, especially in the case of relatively low sampling frequency. Furthermore, not every digital control algorithm can be modeled accurately using continuous-time transfer functions. To improve the accuracy and generality of the admittance models, the discrete nature of the control system can be recognized, e.g., as in [13], by modeling the control system as a discrete-time system while maintaining the continuous characteristic of the rest of the system. Furthermore, purely discrete-time models have also been employed to examine the output admittance as observed by the converter control system [14]–[16]. However, these models do not describe the true output admittance of the system, especially at higher frequencies and above the Nyquist frequency.

In the majority of admittance modeling methods, including those used in [6]–[13], the hold interface is modeled to a varying degree of accuracy, but the sampler is neglected. The characteristics of sampling have been considered only in a few recent works [17], [18], where sampling is modeled as impulse modulation that creates additional components, called images, to the sampled signal [19].

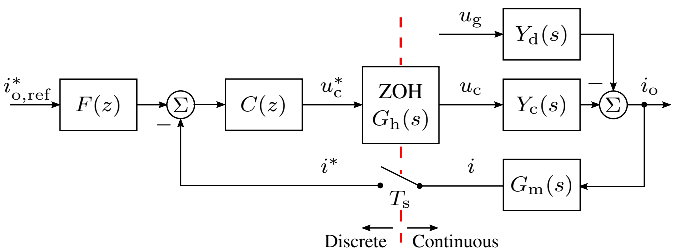

Fig. 2. Block diagram of a current-controlled converter system.

In [17], a multi-variable high-frequency modeling method was proposed to model the admittance of a converter accurately for frequencies above the control bandwidth of the converter. The system was presented as an infinite-dimensional matrix in the frequency domain, and the admittance of the converter was obtained by approximating the infinite-dimensional admittance matrix by a finite submatrix consisting of its most significant components. However, several restrictive assumptions, such as limiting the model to frequencies above the controller bandwidth, were made in the derivation of the method in [17] that hinder its generality. Additionally, the presented method was not compared to the existing admittance modeling methods.

In [18], a multiple-frequency modeling method was proposed that accounts for the images created in the sampling process. The derivation of the multiple-frequency model is based on the manipulation of a hybrid output admittance model, i.e., a model where the controller is modeled as a discrete-time system and the plant as a continuous-time system, similarly as in [13]. The resulting model is accurate for a wide range of frequencies, but contains an infinite sum. The practical implementation of this infinite sum is challenging, and it has been approximated by truncating the sum to some finite number of terms. This corresponds to approximating the infinite-dimensional admittance matrix in [17] by a finite submatrix.

This paper presents a systematic modeling method for the converter output admittance, which is obtained by applying inter-sample modeling theory of sampled-data systems. Inter-sample modeling can be used to analyze the response of a digital control system in-between the sampling instants [20]. The contributions of this paper can be summarized as follows.

1) The proposed inter-sample modeling method improves the modeling accuracy as compared to the conventional continuous-time [6]–[12], discrete-time [14]–[16], and hybrid [13] modeling methods.
2) The presented method circumvents the inclusion of the impractical infinite sums present in [17] and [18] by using a single transfer function for a compact, yet exact representation. This is accomplished by using a relation between Laplace and Z-transforms.
3) The proposed method is compared to the state-of-the-art methods, used, e.g., in [6]–[18], by means of analysis and simulations. Additionally, the relations between the apparently different modeling methods [13], [17], [18] are clarified. System properties for which the presented method yields notable increase in accuracy, as compared to the conventional methods, are analyzed and presented.
4) The proposed method is validated by means of simulations experiments, also above the Nyquist frequency.

Inter-sample modeling enables the use of discrete-time control algorithms directly in the model, improving its generality over the purely continuous-time modeling [6]–[12] while being more suitable for output admittance modeling as compared to the purely discrete-time modeling [14]–[16]. Thus, systems employing control designs with no continuous-time counterpart (e.g., deadbeat control) can be effortlessly and accurately modeled.

II. Interface Models

In this paper, a current-controlled converter system shown in Fig. 2 is used as an example. The system shown in Fig. 2 consists of a reference prefilter $F(z)$, feedback controller $C(z)$, hold interface $G_h(s)$, sampler represented by a switch, the open-loop admittances $Y_c(s)$ and $Y_d(s)$ of the controlled plant, and measurement interface $G_m(s)$. Typically, the measurement interface includes an analog filter with low-pass filter characteristics. Furthermore, i_o is the controlled current, i is the measured current, and $i^*_{o,ref}$ and u_g are the reference and disturbance inputs, respectively. The system in Fig. 2 could represent, e.g., the grid converter shown in Fig. 1. In that case, the current source is $i_s(s) = G_{cl}(s) i^*_{o,ref}(s)$, where $G_{cl}(s)$ is the closed-loop reference tracking transfer function. The positive direction of i_o is defined from the converter towards the output terminals, as in Fig. 1. The asterisk in the symbols denotes that the corresponding signal or transfer function is sampled. In this paper, complex and real transfer functions are not distinguished from one another, as the presented theory is applicable in both cases.

To limit the content, only current-controlled converters are considered. However, the proposed method is also directly applicable to, e.g., analysis of output impedance of ac voltage controlled converters [21], [22]. Likewise, other control schemes that can be represented by a reference prefilter $F(z)$ and a feedback controller $C(z)$ in Fig. 2 can be analyzed in an analogous manner as well. Additional signal paths from the disturbance input can be accounted for in the admittance model, as exemplified in Section V. Next, the models used for sampling and hold are presented.

A. Sampling

The process of sampling is modeled using impulse modulation [19]. In impulse modulation, the input signal is modulated by an infinite series of Dirac delta functions, i.e., a Dirac comb. As a result, the output of the sampler is a continuous function

$$i^*(t) = T_s \sum_{k=0}^{\infty} i(t)\delta(t - kT_s) \tag{1}$$

where T_s is the sampling period and δ is the Dirac delta function. Scaling by T_s is done to match the unit of i^* with that of i. The signal $i(t)$ is assumed to vanish for negative t and thus the sum in (1) starts from zero. By applying the Laplace transform $\mathcal{L}\{\cdot\}$ on the sampled signal $i^*(t)$, one obtains

$$i^*(s) = \mathcal{L}\{i^*(t)\} = T_\mathrm{s} \sum_{k=0}^{\infty} i(kT_\mathrm{s})\mathrm{e}^{-skT_\mathrm{s}} \tag{2}$$

where the sifting property [19] of the Dirac delta function was used. The above transformation is defined as the starred transform of the signal $i(t)$, i.e., it gives the frequency characteristics of the sampled version of the signal. In fact, one can recognize the equation to be a scaled version of the one-side Z-transform of the signal i with $z = \exp(sT_\mathrm{s})$, i.e., $i^*(s) = i(z)|_{z=\exp(sT_\mathrm{s})}$ [23]. An alternative representation of the starred transform can be found by applying the Poisson summation rule [23], which yields the starred transform as

$$i^*(s) = \sum_{k=-\infty}^{\infty} i(s + \mathrm{j}k\omega_\mathrm{s}) \tag{3}$$

where $\omega_\mathrm{s} = 2\pi/T_\mathrm{s}$ is the sampling angular frequency. The above equation reveals that the sampling operation transforms the spectrum of the signal periodic with period ω_s, i.e., $i^*(s) = i^*(s + \mathrm{j}k\omega_\mathrm{s})\ \forall k \in \mathbb{Z}$.

In the derivation of the admittance model presented in Section III, starred transforms of the products of transfer functions and signals are required. In case either the signal or the transfer function is already periodic with ω_s, the starred transform is simply equal to the product of the starred transforms, e.g.,

$$\left[Y(s)G_\mathrm{h}(s)u_\mathrm{c}^*(s)\right]^* = \left[Y(s)G_\mathrm{h}(s)\right]^* u_\mathrm{c}^*(s) \tag{4}$$

where

$$Y(s) = G_\mathrm{m}(s)Y_\mathrm{c}(s) \tag{5}$$

and where both of the starred transforms are defined according to (3). However, if neither the signal nor the transfer function is periodic, the signal becomes time-variant and the starred transform needs to be applied on the whole product, e.g., $[G_\mathrm{m}(s)Y_\mathrm{d}(s)u_\mathrm{g}(s)]^* \neq [G_\mathrm{m}(s)Y_\mathrm{d}(s)]^* u_\mathrm{g}^*(s)$ [19].

B. Hold

The voltage reference output by the controller is typically maintained constant between sampling instants. Assuming that the modulator can perfectly realize its input reference and that the switching frequency harmonics are disregarded, the effect of the modulator can be neglected. As a result, the translation from the voltage reference to the realized voltage can be modeled with the zero-order hold (ZOH) [24]

$$G_\mathrm{h}(s) = \frac{1 - \mathrm{e}^{-sT_\mathrm{s}}}{sT_\mathrm{s}} \tag{6}$$

which is used in this paper to model the hold. However, the aforementioned assumptions do not generally hold and thus more accurate models have been developed, e.g., [25], [26]. These more advanced models of the hold interface may also be employed in the modeling instead of the ZOH.

It is also of interest to examine the starred transform $[Y(s)G_\mathrm{h}(s)]^*$ of the product of the measurement interface G_m, the open-loop admittance Y_c, and the hold G_h, cf. (4) and (5). The numerator of the ZOH is ω_s periodic, so it can be factored out of the transform, leading to

$$\left[Y(s)G_\mathrm{h}(s)\right]^* = (1 - \mathrm{e}^{-sT_\mathrm{s}}) \left[\frac{Y(s)}{sT_\mathrm{s}}\right]^*. \tag{7}$$

Since $[Y(s)/sT_\mathrm{s}]^*$ can be expressed as an infinite sum of samples obtained from the unit step response of $Y(s)/T_\mathrm{s}$ according to (2), this result is actually equivalent to the step-invariant Z-transform of $Y(s)$

$$\left[Y(s)G_\mathrm{h}(s)\right]^* = Y(z) = (1 - z^{-1})\mathcal{Z}\left\{\mathcal{L}^{-1}\left\{\frac{Y(s)}{s}\right\}_{t=kT_\mathrm{s}}\right\} \tag{8}$$

where $\mathcal{L}^{-1}\{\cdot\}$ is the inverse Laplace transform, $\mathcal{Z}\{\cdot\}$ is the Z-transform, and where the identity

$$z = \exp(sT_\mathrm{s}) \tag{9}$$

is applied. The relation (8) is employed in the following section for deriving the proposed output admittance model.

III. Output Admittance Models

In this section, the proposed inter-sample admittance modeling method is applied to obtain an output admittance model for the example system shown in Fig. 2. In addition, the other admittance models used for comparison are presented. In the following, a linear system with constant parameters is assumed. A non-linear model extension is discussed in Section V. Operating point dependency of the parameters, e.g., inductances, can be taken into account by employing the models presented in this section at a specific operating point.

A. Inter-Sample Model

From Fig. 2, the following relations between different signals can be written:

$$u_\mathrm{c}(s) = G_\mathrm{h}(s)C(z)\left[F(z)i_\mathrm{o,ref}^*(s) - i^*(s)\right] \tag{10}$$

$$i(s) = G_\mathrm{m}(s)\left[Y_\mathrm{c}(s)u_\mathrm{c}(s) - Y_\mathrm{d}(s)u_\mathrm{g}(s)\right] \tag{11}$$

$$i_\mathrm{o}(s) = \frac{i(s)}{G_\mathrm{m}(s)} \tag{12}$$

where the relation (9) is used to map the controller pulse-transfer functions into the Laplace domain. Placing (10) into (11) and employing (5), one obtains

$$i(s) = L(s)\left[F(z)i_\mathrm{o,ref}^*(s) - i^*(s)\right] - G_\mathrm{m}(s)Y_\mathrm{d}(s)u_\mathrm{g}(s) \tag{13}$$

where the current i appears both in continuous and sampled form and where

$$L(s) = Y(s)G_\mathrm{h}(s)C(z) \tag{14}$$

is the loop gain of the system. The sampled form i^* can be solved by applying the starred transform on both sides of (13) and solving for i^* by applying identities (4) and (8). This yields

$$i^*(s) = \frac{Y(z)C(z)F(z)i_\mathrm{o,ref}^*(s) - \left[G_\mathrm{m}(s)Y_\mathrm{d}(s)u_\mathrm{g}(s)\right]^*}{1 + Y(z)C(z)} \tag{15}$$

which can be recognized as the system seen by the discrete-time controller. By placing (15) into (13), one obtains

$$i(s) = \frac{L(s)F(z)i^*_{\mathrm{o,ref}}(s)}{1+Y(z)C(z)} + \frac{L(s)\left[G_{\mathrm{m}}(s)Y_{\mathrm{d}}(s)u_{\mathrm{g}}(s)\right]^*}{1+Y(z)C(z)} - G_{\mathrm{m}}(s)Y_{\mathrm{d}}(s)u_{\mathrm{g}}(s). \tag{16}$$

By applying the identity (3) to $[G_{\mathrm{m}}(s)Y_{\mathrm{d}}(s)u_{\mathrm{g}}(s)]^*$ in (16) and separating the $k=0$ component from the sum, one obtains

$$\begin{aligned} i(s) &= \frac{L(s)F(z)}{1+Y(z)C(z)} i^*_{\mathrm{o,ref}}(s) \\ &\quad - \underbrace{\left[1 - \frac{L(s)}{1+Y(z)C(z)}\right] Y_{\mathrm{d}}(s)}_{\text{Output admittance}} G_{\mathrm{m}}(s)u_{\mathrm{g}}(s) \\ &\quad + \underbrace{\frac{L(s)\sum_{\substack{k=-\infty \\ k\neq 0}}^{\infty} Y(s+\mathrm{j}k\omega_{\mathrm{s}})u_{\mathrm{g}}(s+\mathrm{j}k\omega_{\mathrm{s}})}{1+Y(z)C(z)}}_{\text{Current component created by images}}. \end{aligned} \tag{17}$$

The infinite sum in (17) shows the effect of images formed in the sampler. The model for the output admittance $Y_{\mathrm{oa}}(s)$, which describes the system dynamics from the input $u_{\mathrm{g}}(s)$ to the output $i_{\mathrm{o}}(s)$, can then be obtained from (17) by using (12) as

$$Y_{\mathrm{oa}}(s) = \frac{i_{\mathrm{o}}(s)}{u_{\mathrm{g}}(s)} = Y_{\mathrm{d}}(s) - \frac{L(s)Y_{\mathrm{d}}(s)}{1+Y(z)C(z)} \tag{18}$$

which consists of the open-loop admittance $Y_{\mathrm{d}}(s)$ of the plant and the admittance shaping effect of the control system. Furthermore, (17) can also be used to analyze the admittances of images by examining individual terms of the infinite sum.

Remark: An equivalent form of (18) can be derived using the multiple-frequency modeling method presented in [18] with the difference that $Y(z)$ is represented by an infinite sum, i.e., it is written as

$$Y(z) = \sum_{k=-\infty}^{\infty} Y(s+\mathrm{j}k\omega_{\mathrm{s}})G_{\mathrm{h}}(s+\mathrm{j}k\omega_{\mathrm{s}}). \tag{19}$$

Thus, if the output admittance of the example system were written using the modeling method of [18], one would obtain

$$Y_{\mathrm{oa}}(s) = Y_{\mathrm{d}}(s) - \frac{L(s)Y_{\mathrm{d}}(s)}{1+\sum_{k=-\infty}^{\infty} Y(s+\mathrm{j}k\omega_{\mathrm{s}})G_{\mathrm{h}}(s+\mathrm{j}k\omega_{\mathrm{s}})C(z)}. \tag{20}$$

The practical implementation of the infinite sum in the above expression is not elaborated in [18]. A feasible approximation is to truncate the sum to a finite number of terms, as explained in [17]. On the other hand, the above-mentioned sum is recognized as the step-invariant Z-transform of $Y(s)$ [cf. (8)] in the proposed inter-sample modeling approach. This results in a compact and exact representation of the sum without the need for approximation.

Furthermore, it can be shown that the diagonal elements of the more general sampled-data frequency response operator presented in [27] also yield a model equivalent to (18). The modeling method presented in [17] follows the frequency response operator approach, but it does not result in an equivalent model. In addition, due to the relatively strict assumptions made in the modeling in [17], the applicability of the resulting admittance model is limited, as accuracy cannot be guaranteed in general. On the other hand, no corresponding assumptions are made in the proposed inter-sample model, which makes it more general. Out of the equivalent models, (18) is the simplest to present and apply in practice.

B. Single-Frequency Model

The single-frequency admittance model has been used, e.g., in [13], [18]. It can be obtained as a simplification of the inter-sample model (18) by assuming the sampling process linear. This can be seen by neglecting the images created by sampling in (3). As a result, the sum in (19) reduces to $Y(s)G_{\mathrm{h}}(s)$, and thus (18) reduces to

$$Y^{\mathrm{sf}}_{\mathrm{oa}}(s) = \frac{Y_{\mathrm{d}}(s)}{1+Y(s)G_{\mathrm{h}}(s)C(z)} \tag{21}$$

which is defined as the single-frequency admittance in [18].

C. Continuous-Time Model

The continuous-time model has been used, e.g., in [7]–[9]. It is a more conventional model, where the control system of the converter is assumed to be continuous-time. The hold interface is modeled as a ZOH and the sampler is disregarded [7]–[9]. With the assumption of a continuous-time controller, the output admittance is obtained from Fig. 2 as

$$Y^{\mathrm{c}}_{\mathrm{oa}}(s) = \frac{Y_{\mathrm{d}}(s)}{1+Y(s)G_{\mathrm{h}}(s)C^{\mathrm{c}}(s)} \tag{22}$$

where $C^{\mathrm{c}}(s)$ is a continuous-time counterpart of $C(z)$. It is worth noting that the continuous-time counterpart of the controller is not unique, as several different transformation methods are available [19]. A shortcoming of the continuous-time model is that it is not possible to obtain a continuous-time counterpart for every discrete-time controller $C(z)$, e.g., deadbeat controllers.

D. Discrete-Time Model

The discrete-time model has been used, e.g., in [14]–[16]. The output admittance can be written in the discrete-time domain as

$$Y^{\mathrm{d}}_{\mathrm{oa}}(z) = \frac{Y_{\mathrm{d}}(z)}{1+Y(z)C(z)} \tag{23}$$

where $Y(z)$ and $Y_{\mathrm{d}}(z)$ are obtained by applying the step-invariant Z-transform (8) on $Y(s)$ and $Y_{\mathrm{d}}(s)$, respectively. The purely discrete-time models describe the behavior of the plant as observed by the converter control system. However, the dynamics observed at the sampling frequency of the converter control system do not coincide with the true dynamics observed at the output terminals, especially at higher frequencies. Furthermore, one severe shortcoming of the purely discrete-time model is that it is periodic with $\omega_{\mathrm{s}}/2$, i.e., the model does not contain any information about the output admittance above the Nyquist frequency. Nevertheless, it has been used to analyze the output admittance for frequencies below the Nyquist frequency [14]–[16].

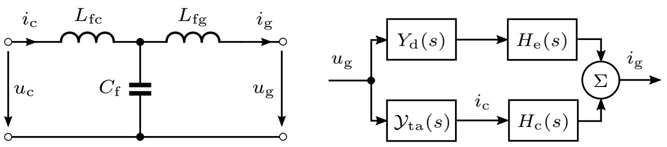

(a) (b)

Fig. 3. (a) Circuit model of an LCL filter. (b) Block diagram of the converter system expressed using transadmittance $\mathcal{Y}_{ta}(s) \in \{Y_{ta}(s), Y_{ta}^{sf}(s), Y_{ta}^{c}(s)\}$ from u_g to i_c.

IV. Comparative Analysis

A. Comparison of the Analytical Models

To compare the proposed model (18) to the models (21)–(23), a single-phase converter system is considered as an example. The plant is assumed to be an ideal LCL filter, i.e., one with no resistive components, shown in Fig. 3(a). The converter-side and grid-side inductances are $L_{fc} = 3.3$ mH and $L_{fg} = 3$ mH, respectively, and the filter capacitance is $C_f = 8.8$ µF. The measurements are assumed ideal, i.e, $G_m(s) = 1$. This simplifies the analysis greatly, as $Y(s) = Y_c(s)$ and $i_o = i$. Two different cases are examined to compare the presented output admittance models.

1) Case 1, Grid Current Measurement: The grid current i_g is selected as the controlled variable, i.e., $i_o = i_g$. The converter is controlled using a proportional–resonant (PR) controller

$$C_{PR}(z) = k_p + \frac{k_i \sin(\omega_i T_s)}{2\omega_i} \frac{z^2 - 1}{z^2 - 2\cos(\omega_i T_s)z + 1} \tag{24}$$

where k_p is the proportional gain, k_i is the resonant gain, and $\omega_i = 2\pi \cdot 50$ rad/s is the resonant angular frequency. A continuous-time counterpart of $C_{PR}(z)$ can be obtained as

$$C_{PR}^{c}(s) = k_p + \frac{k_i s}{s^2 + \omega_i^2} \tag{25}$$

if Tustin transformation with prewarping at the resonant angular frequency ω_i is used [28]. The controller gains are selected as $k_p = 10$ Ω and $k_i = 200$ Ω/s. Furthermore, a computational delay of one sampling period is incurred in the control system, resulting in the controller pulse-transfer function $C(z) = z^{-1} C_{PR}(z)$ and transfer function $C^c(s) = \exp(-sT_s) C_{PR}^{c}(s)$. The relevant open-loop dynamics of the LCL filter can be written as

$$Y_c(s) = \frac{i_g(s)}{u_c(s)} = \frac{1}{C_f L_{fc} L_{fg} s(s^2 + \omega_r^2)} \tag{26}$$

$$Y_d(s) = \frac{i_g(s)}{u_g(s)} = \frac{s^2 + \omega_{ar}^2}{L_{fg} s(s^2 + \omega_r^2)} \tag{27}$$

where $\omega_r = \sqrt{(L_{fc} + L_{fg})/(C_f L_{fc} L_{fg})}$ is the resonance angular frequency and $\omega_{ar} = \sqrt{1/(L_{fc} C_f)}$ is the anti-resonance angular frequency. The sampling frequency is $f_s = 4$ kHz.

A simulation model corresponding to the example system shown in Fig. 2 was built and the output admittance of the system was identified from the model. The comparison of the analytical models (18) and (21)–(23) with the simulation results for Case 1 is shown in Fig. 4. It can be observed that all three models apart from the discrete-time model agree well with the simulations. The discrete-time model matches with the simulations up to frequencies about one tenth of the Nyquist frequency, after which the accuracy of the model deteriorates. The discrete-time model, describing the system characteristics as observed by the converter control system, does not reflect the system response observed at the output terminals, and therefore it is disregarded in further analysis. Despite the similarity of the three models (18), (21), and (22), the result does not generalize, as will be shown in the second example case.

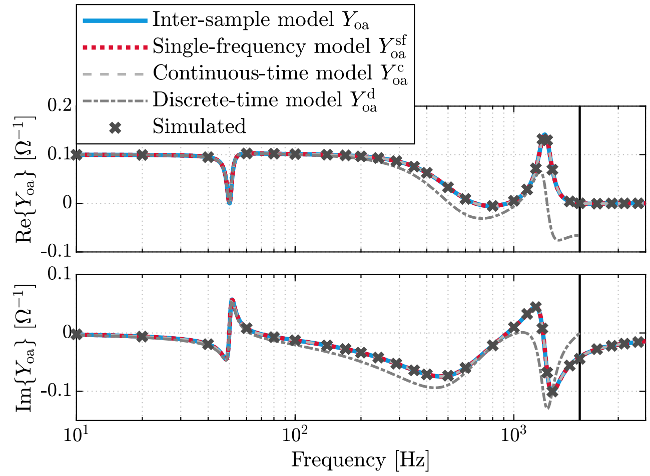

Fig. 4. Comparison of the analytically computed output admittances for Case 1. The black vertical line marks the Nyquist frequency of 2 kHz.

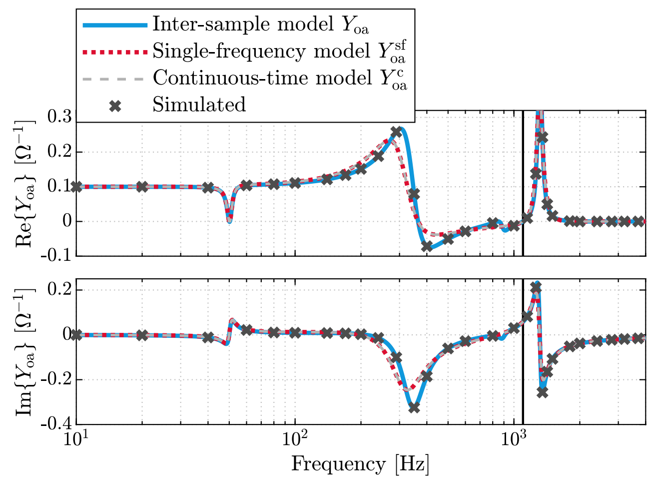

Fig. 5. Comparison of the analytically computed output admittances for Case 2. The black vertical line marks the Nyquist frequency of 1.1 kHz.

2) Case 2, Converter Current Measurement: The converter current i_c is selected as the controlled variable, i.e., $i_o = i_c$, and it is controlled using the same PR controller as in Case 1 with the same gains. The relevant open-loop dynamics of the LCL filter can be written as

$$Y_c(s) = \frac{i_c(s)}{u_c(s)} = \frac{s^2 + \omega_{ar2}^2}{L_{fc} s(s^2 + \omega_r^2)} \tag{28}$$

$$Y_d(s) = \frac{i_c(s)}{u_g(s)} = \frac{1}{C_f L_{fc} L_{fg} s(s^2 + \omega_r^2)} \tag{29}$$

where $\omega_{\mathrm{ar2}} = \sqrt{1/(L_{\mathrm{fg}}C_{\mathrm{f}})}$ is the anti-resonance angular frequency.

Since the controlled variable is the converter current, i.e., $i_{\mathrm{o}} = i_{\mathrm{c}}$, the expressions (18), (21), and (22) yield the converter transadmittances $Y_{\mathrm{ta}}(s)$, $Y_{\mathrm{ta}}^{\mathrm{sf}}(s)$ and $Y_{\mathrm{ta}}^{\mathrm{c}}(s)$ from u_{g} to i_{c}, respectively. These transadmittances can be extended to the output admittances by considering the block diagram in Fig. 3(b) that depicts the system dynamics from u_{g} to i_{g} for Case 2. Each model for the output admittance can thus be obtained similarly, e.g., for the inter-sample model, the expression is

$$Y_{\mathrm{oa}}(s) = \frac{i_{\mathrm{g}}(s)}{u_{\mathrm{g}}(s)} = Y_{\mathrm{ta}}(s)H_{\mathrm{c}}(s) + Y_{\mathrm{d}}(s)H_{\mathrm{e}}(s) \tag{30}$$

where

$$H_{\mathrm{c}}(s) = \frac{i_{\mathrm{g}}(s)}{i_{\mathrm{c}}(s)} = \frac{1}{C_{\mathrm{f}}L_{\mathrm{fg}}(s^2+\omega_{\mathrm{ar2}}^2)} \tag{31}$$

$$H_{\mathrm{e}}(s) = \frac{s^2(s^2+\omega_{\mathrm{ar}}^2+\omega_{\mathrm{ar2}}^2)}{\omega_{\mathrm{ar}}^2(s^2+\omega_{\mathrm{ar2}}^2)}. \tag{32}$$

This case is selected to correspond to a system design proposed in [29], and thus the sampling frequency is $f_{\mathrm{s}} = 2.2$ kHz.

In the simulation model, the converter-side current i_{c} is fed back to the PR controller and the converter output admittance from u_{g} to i_{g} was identified. A comparison of the obtained analytical models with the simulation results for Case 2 is shown in Fig. 5. In this case, the inter-sample model can be seen to agree well with the simulation results whereas the single-frequency and the continuous-time models deviate from the simulation results in the frequency range 200–500 Hz, as can be seen in Fig. 5. As the single-frequency and continuous-time models are practically equivalent, the continuous-time model is disregarded in further analysis. The origins of the differences between the inter-sample and single-frequency models are analyzed below.

B. Analysis of Disparities Between the Inter-Sample and Single-Frequency Models

As both the inter-sample and single-frequency output admittances are extended similarly in Case 2 according to expression (30), it suffices to analyze the differences between the transadmittances $Y_{\mathrm{ta}}(s)$ and $Y_{\mathrm{ta}}^{\mathrm{sf}}(s)$ obtained from (18) and (21). The equation of the inter-sample transadmittance can be written using the single-frequency transadmittance as

$$Y_{\mathrm{ta}}(s) = Y_{\mathrm{ta}}^{\mathrm{sf}}(s)\left\{1 + \big[\underbrace{Y_{\mathrm{c}}(z) - Y_{\mathrm{c}}(s)G_{\mathrm{h}}(s)}_{P_1(s)}\big]\underbrace{C(z)}_{P_2(s)} \cdot \underbrace{\frac{C(z)G_{\mathrm{h}}(s)Y_{\mathrm{c}}(s)}{1+Y_{\mathrm{c}}(z)C(z)}}_{P_3(s)}\right\}. \tag{33}$$

It is evident that the inter-sample admittance depends heavily on the single-frequency admittance. The second term within the curly brackets of (33) dictates the difference between the two admittance models. This term can be divided into three parts that are discussed below.

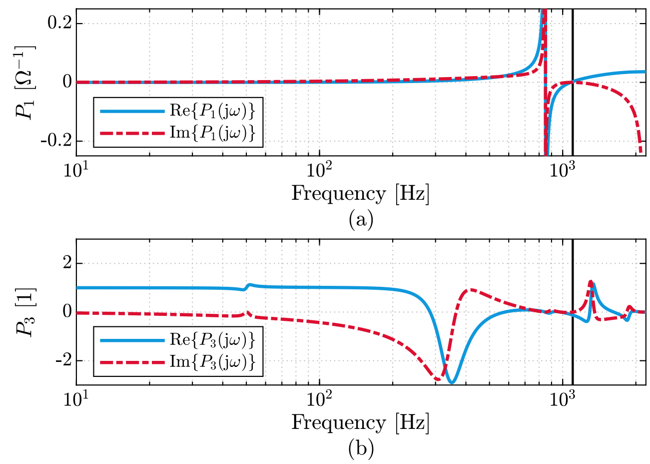

Fig. 6. Frequency responses of the subsystems (a) $P_1(s)$ and (b) $P_3(s)$. The black vertical line marks the Nyquist frequency of 1.1 kHz.

1) Part 1: $P_1(s) = Y_{\mathrm{c}}(z) - Y_{\mathrm{c}}(s)G_{\mathrm{h}}(s)$: This part describes the difference how the controller sees the plant, $Y_{\mathrm{c}}(z)$, and how the plant actually behaves, $Y_{\mathrm{c}}(s)G_{\mathrm{h}}(s)$. This difference is created by the images formed by sampling, i.e.,

$$Y_{\mathrm{c}}(z) - Y_{\mathrm{c}}(s)G_{\mathrm{h}}(s) = \sum_{\substack{k=-\infty \\ k\neq 0}}^{\infty} Y_{\mathrm{c}}(s+\mathrm{j}k\omega_{\mathrm{s}})G_{\mathrm{h}}(s+\mathrm{j}k\omega_{\mathrm{s}}) \tag{34}$$

according to (8). This transfer function, shown in Fig. 6(a), is the most significant source of disparity between the inter-sample and single-frequency models. This error can be substantial when the open-loop transfer functions of the plant, Y_{c} and Y_{d}, do not damp the frequencies above the Nyquist frequency sufficiently, leading to aliasing. Case 2 is an excellent example of such system, as the resonance frequency $f_{\mathrm{r}} = 1.35$ kHz is above the Nyquist frequency $f_{\mathrm{N}} = 1.1$ kHz, which creates significant aliasing around 850 Hz, as seen in Fig. 6(a).

2) Part 2: $P_2(s) = C(z)$: This part itself is not a source of disparity, but it amplifies the effect of the other parts. With a PR-controller, $C(z)$ has approximately constant magnitude k_{p} at frequencies greatly differing from the resonant frequency ω_{i}.

3) Part 3: $P_3(s) = C(z)G_{\mathrm{h}}(s)Y_{\mathrm{c}}(s)/[1+Y_{\mathrm{c}}(z)C(z)]$: The structure of this part corresponds to a sampled-data transfer function defined as the reference gain in [20]. The reference gain is related to the complementary sensitivity function in the discrete-time domain. Thus, the frequency response of this part is typically a unity gain up to a crossover frequency, after which peaks due to underdamped dynamics might occur, followed by a low-pass filter behavior. In Case 2, $P_3(s)$ has an underdamped mode around 300 Hz, as seen in Fig. 6(b).

4) Combination of the Parts: $1 + P_1(s)P_2(s)P_3(s)$: By examining Fig. 5, the largest discrepancy between the models occurs around 300 Hz, caused by the underdamped dynamics in $P_3(s)$ and enabled by the nonzero gain of $P_1(s)$. Furthermore, a slight discrepancy can be observed around 800–900 Hz due to $P_1(s)$. It is only slight due to the high damping by the open-loop plant dynamics at higher frequencies.

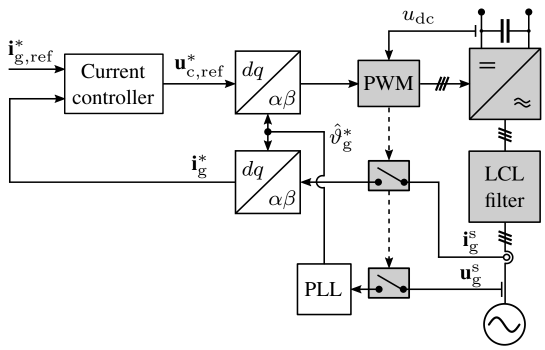

Fig. 7. Block diagram of the three-phase grid converter system. Superscript s indicates that the signal is in stationary coordinates.

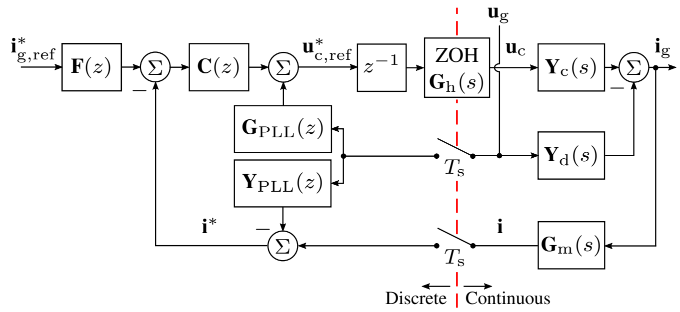

Fig. 8. Block diagram of the linearized model of the grid converter system including the dynamics of the PLL ($\mathbf{G}_{\mathrm{PLL}}$ and $\mathbf{Y}_{\mathrm{PLL}}$) and the current measurement interface ($\mathbf{G}_{\mathrm{m}}$).

Thus, the use of inter-sample model (18) is encouraged in certain cases due to the improved accuracy it provides as compared to the conventional models, i.e., the single-frequency and continuous-time models. In these cases, the damping of the plant is low above the Nyquist frequency, e.g., due to high-frequency grid resonances or special filter design such as that in [29], and underdamped dynamics are present in the complementary sensitivity function, e.g., due to parameter uncertainties. Otherwise, similar accuracy can be expected as with the single-frequency model and the continuous-time model.

V. Three-Phase Output Admittance

A. Model Extension

If additional components, such as the phase-locked loop (PLL) or the direct-voltage controller, are introduced into the control system, the proposed model has to be extended. In this paper, a three-phase system equipped with a PLL is used in the experiments to demonstrate the model extension, cf. Fig. 7.

Due to the PLL, the converter output admittance becomes *dq* unsymmetric [30] and thus it is modeled in synchronous coordinates. The relevant transfer functions can be translated into synchronous coordinates rotating at the grid angular frequency ω_{g} by replacing the s-domain variable with $s+\mathrm{j}\omega_{\mathrm{g}}$, e.g., the ZOH $G_{\mathrm{h}}(s)$ in synchronous coordinates can be obtained as $G_{\mathrm{h}}(s+\mathrm{j}\omega_{\mathrm{g}})$. For *dq* unsymmetric systems, it is more convenient to represent space vectors as column vectors, e.g., the grid current in synchronous coordinates is given by $\mathbf{i}_{\mathrm{g}} = [i_{\mathrm{gd}}, i_{\mathrm{gq}}]^{\mathrm{T}}$. Analogously, transfer functions are represented using 2×2 transfer function matrices denoted by upright boldface letters, e.g., the transfer function matrix of the ZOH in synchronous coordinates is denoted by $\mathbf{G}_{\mathrm{h}}(s)$. Transformation of transfer functions into transfer function matrices is presented alongside the transfer function matrices of the PLL dynamics in Appendix A.

The block diagram of the linearized model of the grid converter system, including dynamics of the PLL, is shown in Fig. 8. Similarly as in Fig. 2, $\mathbf{Y}(s)$ and $\mathbf{Y}_{\mathrm{d}}(s)$ are the open-loop plant dynamics, $\mathbf{C}(z)$ is the feedback controller, $\mathbf{F}(z)$ is the reference prefilter, and $\mathbf{G}_{\mathrm{m}}(s)$ models the dynamics of the current measurement interface. On top of that, the PLL adds two signal paths from the grid voltage $\mathbf{u}_{\mathrm{g}}$ to the system through transfer function matrices $\mathbf{Y}_{\mathrm{PLL}}(z)$ and $\mathbf{G}_{\mathrm{PLL}}(z)$. Carrying out the block diagram algebra similarly to what was done in Section III, one obtains the inter-sample output admittance of the system, including the PLL, as

$$\begin{aligned}\mathbf{Y}_{\mathrm{oa}}(s) = \big[&-\mathbf{G}_{\mathrm{m}}^{-1}(s)\mathbf{L}(s)\mathbf{Y}_{\mathrm{PLL}}(z) - \mathbf{Y}_{\mathrm{c}}(s)\mathbf{G}_{\mathrm{h}}'(s)\mathbf{G}_{\mathrm{PLL}}(z)\\ &+\mathbf{Y}_{\mathrm{d}}(s)\big] - \big[\mathbf{I}+\mathbf{L}^{*}(s)\big]^{-1}\mathbf{L}(s)\mathbf{G}_{\mathrm{m}}^{-1}(s)\big\{\mathbf{G}_{\mathrm{m}}(s)\mathbf{Y}_{\mathrm{d}}(s)\\ &-\big[\mathbf{Y}(s)\mathbf{G}_{\mathrm{h}}'(s)\big]^{*}\mathbf{G}_{\mathrm{PLL}}(z) - \mathbf{L}^{*}(s)\mathbf{Y}_{\mathrm{PLL}}(z)\big\}\end{aligned} \tag{35}$$

where $\mathbf{G}_{\mathrm{h}}'(s) = z^{-1}\mathbf{G}_{\mathrm{h}}(s)$, $\mathbf{L}(s) = \mathbf{Y}(s)\mathbf{G}_{\mathrm{h}}'(s)\mathbf{C}(z)$, $\mathbf{L}^{*}(s) = \mathbf{Y}(z)\mathbf{C}(z)$, and where $\mathbf{Y}_{\mathrm{PLL}}(z)$ and $\mathbf{G}_{\mathrm{PLL}}(z)$ are defined in Appendix A.

It is worth noting that the effect of the PLL on the proposed model is the same as for the conventional models, i.e., it shapes the Y_{dq} and Y_{qq} elements in the lower frequency range, starting from 0 Hz [12]. The range of the frequencies affected by the PLL in the aforementioned admittance elements is determined by the bandwidth of the PLL. For further analysis on the effect of the PLL on the converter admittance, the interested reader is referred to [12] and the papers cited therein.

B. Measurement Method

The admittance is identified from the system based on measurements of the grid voltages and the grid currents. In the admittance matrix (35), there are four unknown elements. Therefore, at least two separate measurements with linearly independent injections are required [3]. In the case of *dq* unsymmetric system, a natural choice is to apply the injection to d- and q-axes. The relation between the measured currents and voltages for the separate measurements can be expressed as

$$\begin{bmatrix} i_{\mathrm{d}n}(s) \\ i_{\mathrm{q}n}(s)\end{bmatrix} = \begin{bmatrix} Y_{\mathrm{dd}}(s) & Y_{\mathrm{dq}}(s) \\ Y_{\mathrm{qd}}(s) & Y_{\mathrm{qq}}(s)\end{bmatrix}\begin{bmatrix} u_{\mathrm{d}n}(s) \\ u_{\mathrm{q}n}(s)\end{bmatrix} \tag{36}$$

where n is the measurement number. Assuming the system to be time-invariant, the elements of the admittance matrix do not change between the injections. Under this assumption, the admittance matrix can be computed based on two sets of measurements as

$$\begin{bmatrix} Y_{\mathrm{dd}}(s) & Y_{\mathrm{dq}}(s) \\ Y_{\mathrm{qd}}(s) & Y_{\mathrm{qq}}(s)\end{bmatrix} = \begin{bmatrix} i_{\mathrm{d1}}(s) & i_{\mathrm{d2}}(s) \\ i_{\mathrm{q1}}(s) & i_{\mathrm{q2}}(s)\end{bmatrix}\begin{bmatrix} u_{\mathrm{d1}}(s) & u_{\mathrm{d2}}(s) \\ u_{\mathrm{q1}}(s) & u_{\mathrm{q2}}(s)\end{bmatrix}^{-1}. \tag{37}$$

In order to obtain accurate measurement data for a wide range of frequencies, the injected signal needs to be carefully

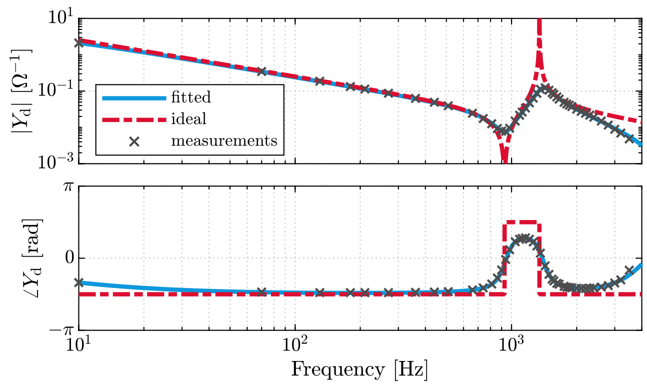

Fig. 9. Experimentally measured open-loop frequency response $Y_\mathrm{d}(\mathrm{j}\omega) = i_\mathrm{g}(\omega)/u_\mathrm{g}(\omega)$ of the the LCL filter and the frequency responses of the fitted transfer function and its corresponding ideal version (27).

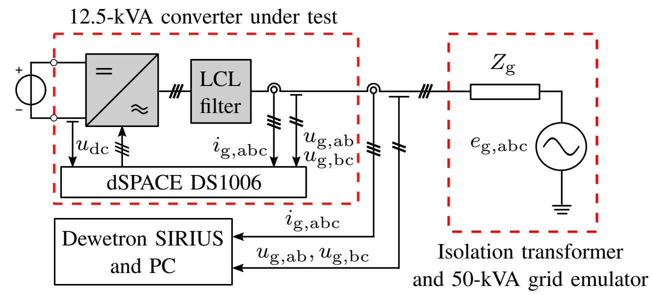

Fig. 10. Block diagram of the experimental setup.

TABLE I
NOMINAL PARAMETERS OF THE GRID CONVERTER SYSTEM

Parameter	Value	Parameter	Value
u_g	$\sqrt{2/3}\cdot 400$ V (1 p.u.)	L_fc	3.3 mH (0.081 p.u.)
ω_g	$2\pi\cdot 50\ \frac{\mathrm{rad}}{\mathrm{s}}$ (1 p.u.)	C_f	8.8 µF (0.035 p.u.)
i_n	$\sqrt{2}\cdot 18$ A (1 p.u.)	L_fg	3 mH (0.073 p.u.)
u_dc	650 V (2 p.u.)	$f_\mathrm{s} = f_\mathrm{sw}$	4 kHz (80 p.u.)
$i_\mathrm{gd,ref}$	10.4 A (0.4 p.u.)	$i_\mathrm{gq,ref}$	0 A (0 p.u.)

selected. Due to the nonlinear behavior of sampling and other system nonlinearities [31], choice of excitation signal has a major effect on the measurement result. To minimize the effect of these nonlinearities, wideband excitation signals should be avoided. Therefore, a single-sine excitation method is used. In this method, a single sinusoid is superimposed on the PCC voltage at a time and the output admittance of the system is computed for that frequency. The single-sine excitation yields highest possible signal-to-noise ratio and thus the most reliable and accurate measurement results [32].

VI. Experimental Validation

The proposed inter-sample modeling method is validated experimentally by measuring the output admittance of a 50-Hz 12.5-kVA three-phase converter equipped with an LCL filter shown in Fig. 7. The nominal system parameters of the available experimental setup are given in Table I. The grid converter was controlled using a state-feedback current controller with a full-order current-type observer, which is similar to the current controller in [14]. The current controller and the derivation of the controller pulse-transfer function matrix $\mathbf{C}(z)$ are presented in Appendix B. The gains of the SRF-PLL were calculated as $k_\mathrm{pp} = 2\zeta_\mathrm{PLL}\omega_\mathrm{PLL}/u_\mathrm{g}$ and $k_\mathrm{ip} = \omega_\mathrm{PLL}^2/u_\mathrm{g}$, where $\omega_\mathrm{PLL} = 2\pi\cdot 20$ rad/s and $\zeta_\mathrm{PLL} = 1/\sqrt{2}$. The current measurement interface of the experimental setup was modeled as a simple first-order low-pass filter, i.e., $G_\mathrm{m}(s) = 1/(\tau s+1)$ with $\tau = 22$ µs. This transfer function was translated to synchronous coordinates and then transformed into a transfer function matrix $\mathbf{G}_\mathrm{m}(s)$ (cf. Appendix A).

For the analytical model (35), the open-loop frequency responses $Y_\mathrm{c}(\mathrm{j}\omega)$ and $Y_\mathrm{d}(\mathrm{j}\omega)$ of the LCL filter were measured, and transfer functions were fitted on the measurements. These fitted transfer functions were transformed into synchronous coordinates and finally into the transfer function matrices $\mathbf{Y}(s)$ and $\mathbf{Y}_\mathrm{d}(s)$ to be employed in (35). The measured frequency response and the frequency responses of the fitted and the ideal transfer functions of $Y_\mathrm{d}(s)$ are shown in Fig. 9.

A block diagram of the experimental setup is presented in Fig. 10. The control algorithm is implemented on a dSPACE DS1006 processor board. The test converter only controls the grid current while another back-to-back connected converter provides dc-link voltage regulation. A 50-kVA three-phase four-quadrant power supply (Regatron TopCon TC.ACS) is used for generating the excitation signals superimposed with the fundamental grid voltage. The grid current and voltage measurements are obtained using a data acquisition device (Dewetron SIRIUS) with sampling frequency of 1 MHz. The fundamental-frequency grid voltage angle is required for measuring the output admittance in synchronous coordinates. It is estimated with a PLL from the line voltage measurements. The bandwidth of this PLL is set very low, 1 Hz, to minimize its effect on the admittance measurement results. The single-sine excitation is applied from 2 Hz to f_s in variable increments to accommodate the logarithmic scale of frequency. Furthermore, as the measurement sensors are subject to noise, logarithmic averaging [2] of the measurements is used to improve the accuracy of the measured output admittance.

Comparison of the proposed model (35) and the admittance measured from the system is presented in Fig. 11. At low frequencies, i.e., below 50 Hz, the small discrepancies in the phases of the cross-coupling admittances Y_dq and Y_qd originate from two sources. Firstly, the signal-to-noise ratio of the measurements is relatively low at these frequencies due to the very low admittance. Secondly, the effect of the PLL used to transform the measurements into synchronous coordinates is not modeled, which causes additional error [33]. Nevertheless, the proposed model agrees very well with the measurement results for the whole frequency range, also above the Nyquist frequency.

VII. Conclusions

This paper presented a systematic inter-sample modeling method for the converter output admittance. The method is based on modeling the converter system as a sampled-data system, where both continuous- and discrete-time signals exist. The interfaces between these two time domains are modeled

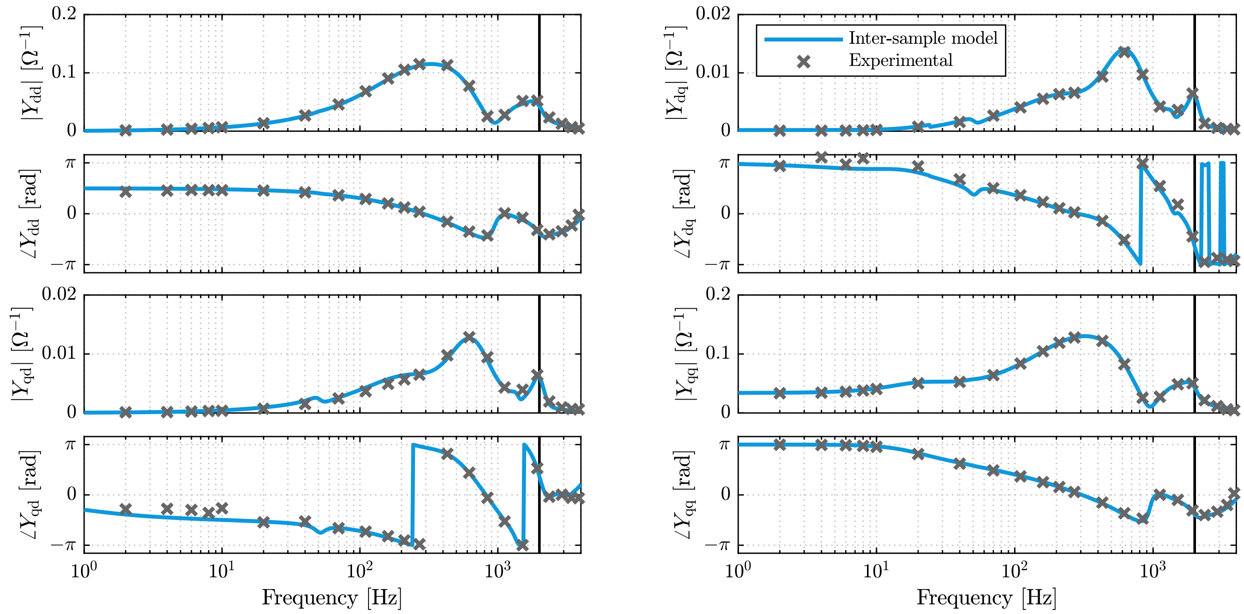

Fig. 11. Experimental comparison of the proposed model and the measured admittance of the system. The black vertical line marks the Nyquist frequency of 2 kHz.

carefully, especially the sampling process. The proposed modeling method is compared to the state-of-the-art admittance modeling methods. It is found to be more accurate than the conventional methods. Out of the methods resulting in equivalent models, the proposed method is found out to be the simplest to present and apply in practice. Furthermore, system properties for which inter-sample modeling yields a notable increase in accuracy, in comparison to the conventional methods, are analyzed and presented. Experimental validation of the proposed method is provided.

Appendix A
Dynamics of the Phase-Locked Loop

By including a synchronous reference frame PLL (SRF-PLL), the system becomes dq unsymmetric [9]. Due to the unsymmetry, complex space vectors are represented using column vectors [30]

$$i_{\mathrm{g}} = i_{\mathrm{gd}} + \mathrm{j} i_{\mathrm{gq}} \longleftrightarrow \mathbf{i}_{\mathrm{g}} = \begin{bmatrix} i_{\mathrm{gd}} \\ i_{\mathrm{gq}} \end{bmatrix}. \tag{38}$$

In addition, the complex transfer functions $Y(s) = Y_{\mathrm{dd}}(s) + \mathrm{j}Y_{\mathrm{qd}}(s)$ are transformed into symmetric transfer function matrices

$$\mathbf{Y}(s) = \begin{bmatrix} Y_{\mathrm{dd}}(s) & Y_{\mathrm{dq}}(s) \\ Y_{\mathrm{qd}}(s) & Y_{\mathrm{qq}}(s) \end{bmatrix} \tag{39}$$

as [30]

$$\begin{aligned} Y_{\mathrm{dd}}(s) = Y_{\mathrm{qq}}(s) = \mathrm{Re}\{Y(s)\} &= \frac{Y(s) + Y^{\dagger}(s)}{2} \\ -Y_{\mathrm{dq}}(s) = Y_{\mathrm{qd}}(s) = \mathrm{Im}\{Y(s)\} &= \frac{Y(s) - Y^{\dagger}(s)}{2} \end{aligned} \tag{40}$$

where the superscript $\dagger$ denotes the complex conjugate operator. By including the dynamics of the PLL in the admittance model, it becomes dependent on the operating point, i.e., it has to be linearized [9]. The dynamic effects of the PLL on the variables transformed in the controller, i.e., $\mathbf{i}_{\mathrm{g}}$ and $\mathbf{u}_{\mathrm{c,ref}}$, are given by [9]

$$\mathbf{i}_{\mathrm{PLL}}(z) = \underbrace{\begin{bmatrix} 0 & -H_{\mathrm{PLL}}(z) i_{\mathrm{gq,0}} \\ 0 & H_{\mathrm{PLL}}(z) i_{\mathrm{gd,0}} \end{bmatrix}}_{\mathbf{Y}_{\mathrm{PLL}}(z)} \begin{bmatrix} u_{\mathrm{gd}}(z) \\ u_{\mathrm{gq}}(z) \end{bmatrix} \tag{41}$$

$$\mathbf{u}_{\mathrm{PLL}}(z) = \underbrace{\begin{bmatrix} 0 & -H_{\mathrm{PLL}}(z) u_{\mathrm{cq,0}} \\ 0 & H_{\mathrm{PLL}}(z) u_{\mathrm{cd,0}} \end{bmatrix}}_{\mathbf{G}_{\mathrm{PLL}}(z)} \begin{bmatrix} u_{\mathrm{gd}}(z) \\ u_{\mathrm{gq}}(z) \end{bmatrix} \tag{42}$$

where $i_{\mathrm{gq,0}}$, $i_{\mathrm{gd,0}}$, $u_{\mathrm{cq,0}}$, and $u_{\mathrm{cd,0}}$ are the component values of $\mathbf{i}_{\mathrm{g}}$ and $\mathbf{u}_{\mathrm{c}}$ at the operating point of the system. The pulse-transfer function of the linearized SRF-PLL is given by [9]

$$H_{\mathrm{PLL}}(z) = \frac{T_{\mathrm{s}}(k_{\mathrm{pp}} z + T_{\mathrm{s}} k_{\mathrm{ip}} - k_{\mathrm{pp}})}{z^2 + (T_{\mathrm{s}} u_{\mathrm{g,0}} k_{\mathrm{pp}} - 2) z + T_{\mathrm{s}} u_{\mathrm{g,0}} (T_{\mathrm{s}} k_{\mathrm{ip}} - k_{\mathrm{pp}}) + 1} \tag{43}$$

where $u_{\mathrm{g,0}}$ is the magnitude of the grid voltage vector at the operating point, and k_{pp} and k_{ip} are the proportional and integral gains of the PLL, respectively.

Appendix B
Current Controller Pulse-Transfer Function $\mathbf{C}(z)$

The state-space model of the LCL filter in synchronous coordinates can be written as

$$\begin{aligned} \mathbf{x}(k+1) &= \mathbf{\Phi} \mathbf{x}(k) + \mathbf{\Gamma}_{\mathrm{c}} u_{\mathrm{c}}(k) + \mathbf{\Gamma}_{\mathrm{g}} u_{\mathrm{g}}(k) \\ i_{\mathrm{g}}(k) &= \mathbf{C}_{\mathrm{g}} \mathbf{x}(k) \end{aligned} \tag{44}$$

where $\mathbf{x} = [i_{\mathrm{c}}, u_{\mathrm{f}}, i_{\mathrm{g}}]^{\mathrm{T}}$ and where u_{f} is the voltage over the filter capacitor. The state matrix $\mathbf{\Phi}$ and the vectors $\mathbf{\Gamma}_{\mathrm{c}}$, $\mathbf{\Gamma}_{\mathrm{g}}$, and $\mathbf{C}_{\mathrm{g}}$ are given in [14]. The controller used in the experiments is very similar to the one presented in [14]. The dynamics of the measurement interface are omitted in the controller design, i.e., $G_{\mathrm{m}}(s) = 1$. The control law of the current controller is

$$\begin{aligned} u_{\mathrm{c,ref}}(k) &= -\mathbf{K}_{\mathrm{a}}\mathbf{x}_{\mathrm{c}}(k) + k_{\mathrm{t}} i_{\mathrm{g,ref}}(k) \\ x_{\mathrm{i}}(k+1) &= x_{\mathrm{i}}(k) + i_{\mathrm{g,ref}}(k) - i_{\mathrm{g}}(k) \end{aligned} \tag{45}$$

where $\mathbf{x}_{\mathrm{c}} = [\hat{i}_{\mathrm{c}}, \hat{u}_{\mathrm{f}}, \hat{i}_{\mathrm{g}}, u_{\mathrm{c}}, x_{\mathrm{i}}]^{\mathrm{T}}$, $\mathbf{K}_{\mathrm{a}}$ is the state feedback gain, and k_{t} is the reference feedforward gain. State variables with hat are estimated using a full-order current-type observer [19]

$$\hat{\mathbf{x}}(k+1) = \mathbf{\Lambda\Phi}\hat{\mathbf{x}}(k) + \mathbf{\Lambda\Gamma}_{\mathrm{c}} u_{\mathrm{c}}(k) + \mathbf{K}_{\mathrm{o}} i_{\mathrm{g}}(k+1) \tag{46}$$

where $\mathbf{K}_{\mathrm{o}}$ is the observer gain and $\mathbf{\Lambda} = \mathbf{I} - \mathbf{K}_{\mathrm{o}}\mathbf{C}_{\mathrm{g}}$. The gains $\mathbf{K}_{\mathrm{a}}, \mathbf{K}_{\mathrm{o}}$, and k_{t} are computed numerically[1], similarly as in [14]. The controller state-space model can be formed based on (44), (45), and (46) as

$$\mathbf{x}_{\mathrm{c}}(k+1) = \mathbf{\Phi}_{\mathrm{c}}\mathbf{x}_{\mathrm{c}}(k) + \mathbf{\Gamma}_1 i_{\mathrm{g}}(k+1) + \mathbf{\Gamma}_2 i_{\mathrm{g}}(k) + \mathbf{\Gamma}_3 i_{\mathrm{g,ref}}(k) \tag{47}$$

where

$$\mathbf{\Phi}_{\mathrm{c}} = \begin{bmatrix} \mathbf{\Lambda\Phi} & \mathbf{\Lambda\Gamma}_{\mathrm{c}} & 0 \\ & -\mathbf{K}_{\mathrm{a}} & \\ \mathbf{0} & 0 & 1 \end{bmatrix} \; \mathbf{\Gamma}_1 = \begin{bmatrix} \mathbf{K}_{\mathrm{o}} \\ 0 \\ 0 \end{bmatrix} \; \mathbf{\Gamma}_2 = \begin{bmatrix} \mathbf{0} \\ 0 \\ -1 \end{bmatrix} \; \mathbf{\Gamma}_3 = \begin{bmatrix} \mathbf{0} \\ k_{\mathrm{t}} \\ 1 \end{bmatrix}. \tag{48}$$

The control law (45) and the controller (47) can be written in the z-domain as

$$\begin{aligned} z\mathbf{x}_{\mathrm{c}}(z) &= \mathbf{\Phi}_{\mathrm{c}}\mathbf{x}_{\mathrm{c}}(z) + (z\mathbf{\Gamma}_1 + \mathbf{\Gamma}_2) i_{\mathrm{g}}(z) + \mathbf{\Gamma}_3 i_{\mathrm{g,ref}}(z) \\ u_{\mathrm{c,ref}}(z) &= -\mathbf{K}_{\mathrm{a}}\mathbf{x}_{\mathrm{c}}(z) + k_{\mathrm{t}} i_{\mathrm{g,ref}}(z). \end{aligned} \tag{49}$$

The controller can be expressed as (cf. Fig. 2)

$$u_{\mathrm{c,ref}}(z) = C(z)[F(z) i_{\mathrm{g,ref}}(k) - i_{\mathrm{g}}(k)] \tag{50}$$

from which the feedback controller $C(z)$ is obtained directly by employing (49) as

$$C(z) = \mathbf{K}_{\mathrm{a}}(z\mathbf{I} - \mathbf{\Phi}_{\mathrm{c}})^{-1}(z\mathbf{\Gamma}_1 + \mathbf{\Gamma}_2). \tag{51}$$

The obtained transfer function can then be transformed into a transfer function matrix $\mathbf{C}(z)$ with (40).

[1]The employed feedback and observer gains are $\mathbf{K}_{\mathrm{a}} = [-2.233 + 0.672\mathrm{j}, 0.177 + 0.007\mathrm{j}, 17.632 - 0.684\mathrm{j}, 0.104 + 0.004\mathrm{j}, -2.797 - 0.443\mathrm{j}]$ and $\mathbf{K}_{\mathrm{o}} = [-0.358 - 0.003\mathrm{j}, -4.255 - 0.336\mathrm{j}, 0.993 - 0.002\mathrm{j}]^{\mathrm{T}}$, respectively. The feedforward gain is $k_{\mathrm{t}} = 3.910 + 0.619\mathrm{j}$.

References

[1] J. Sun, "Impedance-based stability criterion for grid-connected inverters," *IEEE Trans. Power Electron.*, vol. 26, no. 11, pp. 3075–3078, Nov. 2011.

[2] T. Roinila, M. Vilkko, and J. Sun, "Online grid impedance measurement using discrete-interval binary sequence injection," *IEEE Trans. Emerg. Sel. Topics Power Electron.*, vol. 2, no. 4, pp. 985–993, Dec. 2014.

[3] G. Francis, R. Burgos, D. Boroyevich, F. Wang, and K. Karimi, "An algorithm and implementation system for measuring impedance in the DQ domain," in *Proc. IEEE ECCE*, Phoenix, AZ, USA, Sep. 2011, pp. 3221–3228.

[4] Z. Shen, M. Jaksic, P. Mattavelli, D. Boroyevich, J. Verhulst, and M. Belkhayat, "Three-phase AC system impedance measurement unit (IMU) using chirp signal injection," in *Proc. IEEE APEC*, Long Beach, CA, USA, Mar. 2013, pp. 2666–2673.

[5] B. Wen, D. Boroyevich, R. Burgos, P. Mattavelli, and Z. Shen, "Small-signal stability analysis of three-phase AC systems in the presence of constant power loads based on measured dq frame impedances," *IEEE Trans. Power Electron.*, vol. 30, no. 10, pp. 5952–5963, Oct. 2015.

[6] X. Wang, F. Blaabjerg, and W. Wu, "Modeling and analysis of harmonic stability in an AC power-electronics-based power system," *IEEE Trans. Power Electron.*, vol. 29, no. 12, pp. 6421–6432, Dec. 2014.

[7] L. Harnefors, X. Wang, A. G. Yepes, and F. Blaabjerg, "Passivity-based stability assessment of grid-connected VSCs–an overview," *IEEE J. Emerging Sel. Topic Power Electron.*, vol. 4, no. 1, pp. 116–125, Mar. 2015.

[8] B. Wen, D. Dong, D. Boroyevich, R. Burgos, P. Mattavelli, and Z. Shen, "Impedance-based analysis of grid-synchronization stability for three-phase paralleled converters," *IEEE Trans. Power Electron.*, vol. 31, no. 1, pp. 26–38, Jan. 2015.

[9] X. Wang, L. Harnefors, and F. Blaabjerg, "Unified impedance model of grid-connected voltage-source converters," *IEEE Trans. Power Electron.*, vol. 33, no. 2, pp. 1775–1787, Feb. 2018.

[10] J. Sun, "Small-signal methods for AC distributed power systems–a review," *IEEE Trans. Power Electron.*, vol. 24, no. 11, pp. 2545–2554, Nov. 2009.

[11] L. Harnefors, A. G. Yepes, A. Vidal, and J. Doval-Gandoy, "Passivity-based controller design of grid-connected VSCs for prevention of electrical resonance instability," *IEEE Trans. Ind. Electron.*, vol. 62, no. 2, pp. 702–710, Feb. 2015.

[12] B. Wen, D. Boroyevich, R. Burgos, P. Mattavelli, and Z. Shen, "Analysis of DQ small-signal impedance of grid-tied inverters," *IEEE Trans. Power Electron.*, vol. 31, no. 1, pp. 675–687, Jan. 2016.

[13] T. Kato, K. Inoue, and Y. Nakajima, "Stabilization of grid-connected inverter system with feed-forward control," in *Proc. IEEE ECCE*, Cincinnati, OH, USA, Oct. 2017, pp. 3375–3382.

[14] J. Kukkola, M. Hinkkanen, and K. Zenger, "Observer-based state-space current controller for a grid converter equipped with an LCL filter: Analytical method for direct discrete-time design," *IEEE Trans. Ind. Appl.*, vol. 51, no. 5, pp. 4079–4090, Sep./Oct. 2015.

[15] F. M. Rahman, J. Kukkola, V. Pirsto, M. Routimo, and M. Hinkkanen, "State-space control for LCL filters: Comparison between the converter and grid current measurements," in *Proc. IEEE ECCE*, Baltimore, MD, USA, Sep./Oct. 2019, pp. 1491–1498.

[16] E. Rodriguez-Diaz, F. D. Freijedo, J. M. Guerrero, J.-A. Marrero-Sosa, and D. Dujic, "Input-admittance passivity compliance for grid-connected converters with an LCL filter," *IEEE Trans. Ind. Electron.*, vol. 66, no. 2, pp. 1089–1097, Feb. 2019.

[17] F. D. Freijedo, M. Ferrer-Duran, and D. Dujic, "Multi-variable high-frequency input-admittance of grid-connected converters: Modeling, validation and implications on stability," *IEEE Trans. Ind. Electron.*, vol. 66, no. 8, pp. 6505–6515, Aug. 2019.

[18] L. Harnefors, R. Finger, X. Wang, H. Bai, and F. Blaabjerg, "VSC input-admittance modeling and analysis above the Nyquist frequency for passivity-based stability assessment," *IEEE Trans. Ind. Electron.*, vol. 64, no. 8, pp. 6362–6370, Aug. 2017.

[19] G. F. Franklin, J. D. Powell, and M. Workman, *Digital control of dynamic systems*, 3rd ed. Menlo Park, CA: Addison-Wesley, 1998.

[20] G. C. Goodwin and M. Salgado, "Frequency domain sensitivity functions for continuous time systems under sampled data control," *Automatica*, vol. 30, no. 8, pp. 1263–1270, Aug. 1994.

[21] D. Pérez-Estévez, J. Doval-Gandoy, and J. M. Guerrero, "AC-voltage harmonic control for stand-alone and weak-grid-tied converter," *IEEE Trans. Ind. Appl.*, vol. 56, no. 1, pp. 403–421, Jan./Feb. 2020.

[22] X. Wang, P. C. Loh, and F. Blaabjerg, "Stability analysis and controller synthesis for single-loop voltage-controlled VSIs," *IEEE Trans. Power Electron.*, vol. 32, no. 9, pp. 7394–7404, Sep. 2017.

[23] J. R. Ragazzini and L. A. Zadeh, "The analysis of sampled-data systems," *AIEE Trans.*, vol. 71, no. 5, pp. 225–234, Nov. 1952.

[24] S. Buso and P. Mattavelli, *Digital control in power electronics*. Morgan & Claypool Publishers, 2006.

[25] J. Ma, X. Wang, F. Blaabjerg, L. Harnefors, and W. Song, "Accuracy analysis of the zero-order hold model for digital pulse width modulation," *IEEE Trans. Power Electron.*, vol. 33, no. 12, pp. 10 826–10 834, Dec. 2018.

[26] F. Hans, M. Oeltze, and W. Schumacher, "A modified ZOH model for representing the small-signal PWM behavior in digital DC-AC converter systems," in *Proc. IEEE IECON*, Lisbon, Portugal, Oct. 2019, pp. 1514–1520.

[27] Y. Yamamoto and P. P. Khargonekar, "Frequency response of sampled-data systems," *IEEE Trans. Autom. Control*, vol. 41, no. 2, pp. 166–176, Feb. 1996.

[28] A. G. Yepes, F. D. Freijedo, J. Doval-Gandoy, Ó. López, J. Malvar, and P. Fernandez-Comesana, "Effects of discretization methods on the performance of resonant controllers," *IEEE Trans. Power Electron.*, vol. 25, no. 7, pp. 1692–1712, Jul. 2010.

[29] Y. Tang, W. Yao, P. C. Loh, and F. Blaabjerg, "Design of LCL filters with LCL resonance frequencies beyond the Nyquist frequency for grid-connected converters," *IEEE J. Emerging Sel. Topic Power Electron.*, vol. 4, no. 1, pp. 3–14, Mar. 2016.

[30] L. Harnefors, "Modeling of three-phase dynamic systems using complex transfer functions and transfer matrices," *IEEE Trans. Ind. Electron.*, vol. 54, no. 4, pp. 2239–2248, Aug. 2007.

[31] H. Gong, D. Yang, and X. Wang, "Impact of nonlinear dynamics on converter DQ impedance measurement," in *Proc. IEEE COMPEL*, Toronto, ON, Canada, Jun. 2019, pp. 1–6.

[32] T. Roinila, M. Vilkko, and J. Sun, "Broadband methods for online grid impedance measurement," in *Proc. IEEE ECCE*, Denver, CO, USA, Sep. 2013, pp. 3003–3010.

[33] Z. Shen, M. Jaksic, B. Zhou, P. Mattavelli, D. Boroyevich, J. Verhulst, and M. Belkhayat, "Analysis of phase locked loop (PLL) influence on DQ impedance measurement in three-phase AC systems," in *Proc. IEEE APEC*, Long Beach, CA, USA, Mar. 2013, pp. 939–945.

Ville Pirsto received the B.Sc. (Tech.) and M.Sc. (Tech.) degrees in electrical engineering from the Aalto University, Espoo, Finland, in 2017 and 2019, respectively, where he is currently working toward the D.Sc. (Tech.) in electrical engineering.

His current research focuses on grid-connected converters.

Jarno Kukkola received the B.Sc. (Tech.), M.Sc. (Tech.), and D.Sc. (Tech.) degrees in electrical engineering from the Aalto University, Espoo, Finland, in 2010, 2012, and 2017, respectively.

He is currently a Postdoctoral Researcher with the School of Electrical Engineering, Aalto University, Espoo, Finland. His research interests include control systems and grid-connected converters.

Marko Hinkkanen (M'06–SM'13) received the M.Sc.(Eng.) and D.Sc.(Tech.) degrees in electrical engineering from the Helsinki University of Technology, Espoo, Finland, in 2000 and 2004, respectively.

He is currently an Associate Professor with the School of Electrical Engineering, Aalto University, Espoo, Finland. His research interests include control systems, electric drives, and power converters.

Dr. Hinkkanen was the corecipient of the 2016 International Conference on Electrical Machines (ICEM) Brian J. Chalmers Best Paper Award, the 2016 and 2018 IEEE Industry Applications Society Industrial Drives Committee Best Paper Awards, and the 2020 SEMIKRON Innovation Award. He is an Associate Editor for the IEEE TRANSACTIONS ON ENERGY CONVERSION and the *IET Electric Power Applications*.

Lennart Harnefors (S'93-M'97-SM'07-F'17) received the M.Sc., Licentiate, and Ph.D. degrees in electrical engineering from the Royal Institute of Technology (KTH), Stockholm, Sweden, and the Docent (D.Sc.) degree in industrial automation from Lund University, Lund, Sweden, in 1993, 1995, 1997, and 2000, respectively.

Between 1994-2005, he was with Mälardalen University, Västerås, Sweden, from 2001 as a Professor of electrical engineering. Between 2001-2005, he was, in addition, a part-time Visiting Professor of electrical drives with Chalmers University of Technology, Göteborg, Sweden.

In 2005, he joined ABB, HVDC Product Group, Ludvika, Sweden, where, among other duties, he led the control development of the first generation of multilevel-converter HVDC Light. In 2012, he joined ABB, Corporate Research, Västerås, where he was appointed as a Senior Principal Scientist in 2013. In this capacity he coordinates ABB's research in control of power electronic systems. He is, in addition, a part-time Adjunct Professor of power electronics with KTH.

Dr. Harnefors is an Editor of the IEEE Journal of Emerging and Selected Topics in Power Electronics and an Associate Editor of IET Electric Power Applications. His research interests include control and dynamic analysis of power electronic systems, particularly grid-connected converters and ac drives.